Mid-Holocene ITCZ migration: impacts on Hadley cell dynamics and terrestrial hydroclimate

Jianpu Bian[1], Jouni Räisänen[1], and Heikki Seppä[2]

[1]Institute for Atmospheric and Earth System Research, University of Helsinki, Helsinki, Finland
[2]Department of Geosciences and Geography, University of Helsinki, Helsinki, Finland

Correspondence: Jianpu Bian (bian.jianpu@helsinki.fi)

Abstract. This study investigates the multiple changes of the Hadley cell (HC) in response to the northward migration of Intertropical Convergence Zone (ITCZ) and their combined influence on terrestrial hydrological cycle during the mid-Holocene, using simulations from the PMIP4-CMIP6 archive. Our results show that orbital forcing increased radiative heating in the Northern Hemisphere, shifting the ITCZ northward by 0.2° and 0.3° as a multi-model mean using two different precipitation

5   metrics, which is consistent with proxy evidence of a slight northward shift during the mid-Holocene. This migration primarily drives the northward movement of the inner HC edge, resulting in a contracted and weakened northern HC, while the southern HC expands and intensifies. Specifically, the northern HC width contracted by 1.1° and 0.5°, with strength reductions of 3.7% and 4.1%, while the southern HC expanded by 1.2° and 0.6° and strengthened by 2.9% and 1.8%, according to the two streamfunction metrics. Enhanced moisture eddy fluxes are a major contributor to increased terrestrial precipitation in the Northern

10 Hemisphere, particularly in monsoonal regions, while Southern Hemisphere precipitation decreased due to evaporation and dynamic terms. Moist static energy (MSE) budget analysis reveals that stronger rising motion significantly promotes vertical MSE advection over land in the Northern Hemisphere, enhancing moist convection and precipitation, while reduced rising motion weakens vertical MSE advection in the Southern Hemisphere, suppressing moist convection and precipitation. Regionally, ITCZ migration and associated HC changes alter climate patterns with reduced Northern Hemisphere terrestrial aridity and dry-

15 lands contraction, while the Southern Hemisphere has enhanced aridity and drylands expansion. Multiple proxies support these findings, indicating wetter Northern Hemisphere conditions and a drier Southern Hemisphere, although inconsistencies remain in Australia's aridity pattern. Our results highlight the complex interactions among ITCZ migration, Hadley cell dynamics, global hydrological cycle, and terrestrial aridity during the mid-Holocene.

1   Introduction

20 The Hadley cell, characterized by rising air near the equator and descending air in the subtropics, plays a crucial role in regulating the Earth's energy budget by transporting energy from the tropics to higher latitudes (Diaz and Bradley, 2004). The ITCZ is a narrow equatorial band characterized by the convergence of trade winds, intense convective activity, dense cloud cover, and heavy precipitation. As a key component of large-scale atmospheric circulation, the ITCZ is intrinsically connected to the Hadley Cell, with their ascending branches tightly coupled in driving meridional and zonal overturning

25   processes. The ITCZ and Hadley Cell play a pivotal role in shaping precipitation patterns and climate across the tropics and subtropics, significantly influencing monsoonal circulations and the seasonal migration of monsoons and rainfall (Diaz and Bradley, 2004). The positions of both the ITCZ and Hadley cell vary seasonally, following the Sun's migration and changes in Earth's perihelion precession, which have far-reaching effects on global hydrological cycle (Diaz and Bradley, 2004; Kang and Lu, 2012; Kang et al., 2018; Geen et al., 2020; Lionello et al., 2024).

30   During the mid-Holocene (MH; 6,000 years BP), currently arid parts of North Africa were transformed into thriving ecosystems with shrubs, grasslands, and forests (Claussen and Gayler, 1997; Claussen et al., 1999; Holmes, 2008; Harrison et al., 2014; Tierney et al., 2017; Pausata et al., 2020; Thompson et al., 2022; Kaufman and Broadman, 2023). For this warm and humid period characterized by significantly enhanced rainfall, numerous reconstruction and simulation based studies have sought to uncover the drivers behind this remarkable climatic shift (Claussen et al., 2017; Tierney et al., 2017; Pausata et al., 2020;

35   Brierley et al., 2020; Thompson et al., 2022; Kaufman and Broadman, 2023). During the mid-Holocene, increased Northern Hemisphere solar radiation pushed the ITCZ northward beyond its present position (Schneider et al., 2014; Geen et al., 2020; Bian and Räisänen, 2024). This shift can influence the width and intensity of the Hadley cell, strengthen monsoonal circulations and drive a northward expansion and significantly increasing monsoonal rainfall (Diaz and Bradley, 2004; Kang and Lu, 2012; Lionello et al., 2024). Furthermore, these shifts in the ITCZ and Hadley cell had profound effects on regional climates,

40   altering aridity patterns and reshaping biome distributions across the tropics and subtropics (Diaz and Bradley, 2004; Lau and Kim, 2015). Understanding these changes in the Hadley cell and ITCZ is essential for assessing how large-scale circulation shifts drive transformations in the global hydrological cycle across different climate periods.

  Continued from recent advances in understanding the mid-Holocene global ITCZ of Bian and Räisänen (2024), our primary focus for this study is to quantitatively access the influence of the global ITCZ's northward migration on Hadley cell dynamics

45   and their combined impact on the global hydrological cycle and terrestrial aridity during the mid-Holocene. To achieve this, we employ various methods to analyze changes in the Hadley cell and ITCZ between the preindustrial and the mid-Holocene periods. Specifically, we use multiple mass stream-function metrics to assess the edges, width, and intensity of the Hadley cell, along with weighted precipitation metrics to determine the position of the ITCZ (Diaz and Bradley, 2004; Lau and Kim, 2015; Adam et al., 2016; Pikovnik et al., 2022; Lionello et al., 2024). Additionally, we compare our findings with proxy data and

50   investigate the related physical mechanisms through moisture budget and moist static energy (MSE) budget analyses, exploring how these affect global hydrological cycle, terrestrial aridity, and dryland shifts during the mid-Holocene (Bartlein et al., 2011; Prado et al., 2013; Herbert and Harrison, 2016; Hill et al., 2017; Liu et al., 2019; Hill, 2019; Bian and Räisänen, 2024; Lowry and McGowan, 2024; Lionello et al., 2024).

2   Data and Methods

55   ### 2.1   Data

We use monthly outputs of the MH simulations from the the Paleoclimate Modeling Intercomparison Project Phase 4 (PMIP4) (Otto-Bliesner et al., 2017) and the preindustrial (PI) Coupled Model Intercomparison Project Phase 6 (CMIP6) simulations

(Eyring et al., 2016) from nine models (See further model details in Table S1 of the Supplementary material). For this study, we analyze the last 100 years of simulations from each model. The simulations outputs are bilinearly interpolated to a grid resolu-

60 tion of $2.5° \times 2.5°$. For the evaluation of the ITCZ by precipitation metrics and Hadley cell by mass streamfunction metrics, these variables are further bilinearly interpolated into $0.5° \times 0.5°$ and $0.1° \times 0.1°$. Our analysis indicates that differences in grid resolution do not affect the results obviously. Additionally, we incorporate observations of present-day precipitation from the Global Precipitation Climatology Project (GPCP; 1979-2018; Adler et al. (2003)) monthly product to further evaluate the simulations results.

65 We further collect multiple types of reconstructions, and evaluate the PMIP4 simulations against global pollen-based proxies of mean annual precipitation (MAP) and the moisture availability (alpha) index from Bartlein et al. (2011), covering regions of Eurasia, Africa, Europe, and North America. For Australia, we supplement these reconstructions by merging data from the Indo-Pacific Pollen Database (Herbert and Harrison, 2016; Lowry and McGowan, 2024) with additional pollen records (See further details in Tables S2 and S3 of the Supplementary material). Due to the limited pollen records for South America, we

70 further incorporate various types of proxies from Wirtz et al. (2010) and Prado et al. (2013). These proxies include oxygen and carbon isotopic fractionation, along with physical-chemical and biological indicators (Prado et al., 2013).

2.2 Defining metrics for the Hadley cell

We utilize two distinct meridional mass streamfunction ($\Psi(\phi)$) metrics to quantify the zonal and annual edges, as well as the width and strength of the Hadley cell (Diaz and Bradley, 2004; Nguyen et al., 2013; Pikovnik et al., 2022).

75 $$\Psi(\phi) = \frac{2\pi a \cos\phi}{g} \int_0^p [\overline{v}(\phi,p)]\,dp \tag{1}$$

where $[\overline{v}(\phi,p)]$ represents the zonal and time-averaged meridional wind at latitude ϕ, and p is air pressure.

The first Hadley cell edge metric employed is the mid-tropospheric mass streamfunction at 500 hPa (Kang and Lu, 2012; Pikovnik et al., 2022). The southern, inner and northern edge of the Hadley cell are defined as the three latitudes within $40°S$-$40°N$ where the zonal mean mass stream function crosses zero.

80 The mass streamfunction $\Psi(\phi)$ values are negative in the southern Hadley cell branch and positive in the northern Hadley cell branch, increasing poleward with latitude near the shared inner edge where the streamfunction is zero. We further use the maxima (minima) of the meridional mass streamfunction to quantify the strength of the Hadley cell (ϖ_{HC}) as

$$\begin{cases} \varpi_{NHC} = \Psi_{500hPa}|_{max} & \text{for} \quad \phi \in 10°S - 40°N \\ \varpi_{SHC} = \Psi_{500hPa}|_{min} & \text{for} \quad \phi \in 40°S - 10°N \end{cases} \tag{2}$$

where the streamfunction reaches its negative peak in the southern Hadley cell and its positive peak in the northern Hadley

85 cell, respectively. The second Hadley cell edge and intensity metrics are defined analogously with Method I, but using the 900-to-200 hPa average of the streamfunction ($\langle\Psi\rangle_{900-200hPa}$) rather than the value at 500 hPa (Nguyen et al., 2013; Pikovnik et al., 2022).

2.3 Column MSE budget analysis

Previous studies show that moist static energy (MSE) budget plays a critical role in shaping the terrestrial hydrological response
90 to climate change (Hill et al., 2017; Hill, 2019; Geen et al., 2020; Lionello et al., 2024). Here we derive MSE budget terms
from the column total energy budget equation:

$$\frac{\partial A_E}{\partial t} + \nabla \cdot \mathbf{F}_a = R_a + LE + SH_0$$

where A_E is the column total atmospheric energy, consisting of column total potential energy, column kinetic energy, and
column latent energy. $\mathbf{F}_a$ is the column total energy transport: $\langle (MSE + K)\mathbf{V} \rangle$, where $\langle \cdot \rangle$ indicates vertical integration over
95 the mass of column, and $MSE = C_p T + Lq + \Phi$. R_a represents the net energy input: $R_a = R_{TOA} - R_s$, where R_{TOA} and R_s
are the net downward radiative fluxes at the top of the atmosphere (TOA) and the surface, respectively. LE and SH_0 denote the
surface latent and sensible heat fluxes, respectively. Over a long-term time mean, the tendency term approaches zero, and the
column kinetic energy divergence is much smaller compared to the column MSE flux divergence. The time-averaged column
energy budget then becomes

100 $$\nabla \cdot \overline{\mathbf{F}_a} = \overline{R_a} + L\overline{E} + \overline{SH_0} \approx \nabla \cdot \overline{\langle (MSE)\mathbf{V} \rangle} \tag{3}$$

where the vertical energy flux difference between the top and bottom of the atmospheric column is balanced by divergence of
MSE flux (Hill et al., 2017; Hill, 2019):

$$\nabla \cdot \overline{\langle (MSE)\mathbf{V} \rangle} = \langle \overline{\mathbf{V}} \cdot \nabla_p \overline{MSE} \rangle + \langle \overline{\omega} \cdot \frac{\partial}{\partial p} \overline{MSE} \rangle + \nabla \cdot \langle \overline{MSE'\mathbf{V}'} \rangle \tag{4}$$

where $\langle \overline{\mathbf{V}} \cdot \nabla_p \overline{MSE} \rangle$ denotes the column-integrated horizontal MSE advection under time mean, $\langle \overline{\omega} \cdot \frac{\partial}{\partial p} \overline{MSE} \rangle$ the column
105 vertical MSE advection, and $\nabla \cdot \langle \overline{MSE'\mathbf{V}'} \rangle$ the column eddy MSE flux divergence.

For the change of $\nabla \cdot \overline{\mathbf{F}_a}$ from the PI to the MH period,

$$\delta(\nabla \cdot \overline{\mathbf{F}_a}) = \delta \overline{R_a} + L\delta \overline{E} + \delta(\overline{SH_0})$$
$$\approx \langle \delta \left(\overline{\mathbf{V}} \cdot \nabla_p \overline{MSE} \right) \rangle + \langle \delta(\overline{\omega} \cdot \frac{\partial}{\partial p} \overline{MSE}) \rangle + \delta(\nabla \cdot \langle \overline{MSE'\mathbf{V}'} \rangle) \tag{5}$$

where $\delta(\cdot)$ denotes $(\cdot)_{MH} - (\cdot)_{PI}$.
110 Eq. (5) can be further expanded as

$$\delta(\nabla \cdot \overline{\mathbf{F}_a}) \approx \underbrace{\langle \overline{\mathbf{V}} \cdot \nabla_p \delta(\overline{MSE}) \rangle}_{I} + \underbrace{\langle \delta\overline{\mathbf{V}} \cdot \nabla_p \overline{MSE} \rangle}_{II} + \underbrace{\langle \delta\overline{\mathbf{V}} \cdot \nabla_p \delta(\overline{MSE}) \rangle}_{non-linear}$$
$$+ \underbrace{\langle \overline{\omega} \cdot \frac{\partial}{\partial p} \delta(\overline{MSE}) \rangle}_{III} + \underbrace{\langle \delta\overline{\omega} \cdot \frac{\partial}{\partial p} \overline{MSE} \rangle}_{IV} + \underbrace{\langle \delta\overline{\omega} \cdot \frac{\partial}{\partial p} \delta(\overline{MSE}) \rangle}_{non-linear} \tag{6}$$
$$+ \underbrace{\delta(\nabla \cdot \langle \overline{MSE'\mathbf{V}'} \rangle)}_{V}$$

where the last term is evaluated as a residual:

$$\delta(\nabla \cdot \langle \overline{MSE'\mathbf{V'}} \rangle) \approx \delta \overline{R_a} + L\delta \overline{E} + \delta(\overline{SH_0}) - \langle \delta \left(\overline{\mathbf{V}} \cdot \nabla_p \overline{MSE} \right) \rangle - \langle \delta(\overline{\omega} \cdot \frac{\partial}{\partial p} \overline{MSE}) \rangle \qquad (7)$$

As the two non-linear terms of Eq. (6) are minimal, we can approximately get the expression of $\delta(\nabla \cdot \overline{\mathbf{F}_a})$ as:

$$\delta(\nabla \cdot \overline{\mathbf{F}_a}) \approx I + II + III + IV + V \qquad (8)$$

Thus, changes in the MSE budget have five contributing terms in Eq. (8): anomalous column-integrated horizontal advection (thermodynamic term I, and dynamic term II), anomalous column-integrated vertical advection (thermodynamic term III, and dynamic term IV), and anomalous column-integrated eddy MSE flux term V.

The five RHS terms play a critical role in influencing moist convection and precipitation patterns (Hill et al., 2017; Hill, 2019; Lionello et al., 2024). During the mid-Holocene, increased solar radiation modified the meridional thermal contrast in the Northern Hemisphere, altering the MSE gradient and advection, and further enhancing moist convection and precipitation. Horizontal MSE advection is relatively weak in the tropics compared to vertical advection, which has a closer connection with atmospheric energy flux divergence and vertical motion. Vertical MSE advection is primarily driven by the time-mean divergent circulation as a balancing mechanism and is sensitive to the depth of moist convection, which can significantly influence atmospheric instability, the development of convective systems, and changes in precipitation (Back and Bretherton, 2006; Chou et al., 2013; Hill, 2019; Geen et al., 2020; Lionello et al., 2024).

3 Results

3.1 Annual hydrological changes in simulations and reconstructions

During the PI period, the tropics exhibits intense rainfall (≥ 3 mm/day), concentrated primarily between $20°S$ and $20°N$ (Figure 1a), which closely aligns with the observed present-day precipitation patterns from the GPCP dataset (not shown). As illustrated in the Taylor diagram (Taylor (2001); Figure 1c), the PI simulations effectively reproduce the large-scale annual precipitation distribution, showing minimal biases in magnitude and spatial variance when compared to GPCP observations. Notably, the multimodel means outperform most individual models, making them the preferred choice for subsequent analysis. In the zonal-mean framework, the deep tropics are characterized by intense precipitation and strong rising motion, with two distinct peaks centered around $10°S$ and $10°N$ (Figure 1d). During the mid-Holocene, annual precipitation increases significantly in the monsoonal regions and marine subtropics of the Northern Hemisphere (Figure 1b). Additionally, regional marine precipitation increases in the South Pacific and western Indian Ocean, whereas most other tropical ocean regions experience reduced rainfall in the mid-Holocene.

As horizontal advection is relatively weak in the low latitudes, there is a connection between atmospheric energy flux divergence and rising motion by $\nabla \cdot \overline{\mathbf{F}_a} > 0$. This indicates divergence in the upper troposphere and convergence in the lower troposphere, as the total energy content of air typically increases upward. The divergence in the upper troposphere and convergence in the lower troposphere necessitate rising motion in the mid-troposphere. Consequently, increases in precipitation

145   ($\delta P > 0$) are generally associated with an increase in atmospheric energy flux divergence ($\delta \nabla \cdot \overline{\mathbf{F}_a} > 0$), and decreases in $\nabla \cdot \overline{\mathbf{F}_a}$ are usually associated with a decrease in precipitation ($\delta P < 0$). There is a good agreement between the changes in annual precipitation (Figure 1b) and those in the energy flux divergence ($\delta \nabla \cdot \overline{\mathbf{F}_a}$ in Figure 1e).

     The mid-Holocene pollen reconstructions presented by Bartlein et al. (2011) indicate wetter conditions in the Northern Hemisphere (Figure 1f), with increased annual precipitation across tropical and subtropical regions in northern Africa, Europe,

150   East Asia, western and southern North America, which align with the results of the PMIP4 simulations shown in Figure 1b. In contrast, equatorial regions including tropical Africa, experienced reduced rainfall. For the Southern Hemisphere, pollen records indicate wetter conditions in southwestern Africa but a markedly drier climate in southeastern Africa during the mid-Holocene (Figure 1f).

     In South America, multiple types of proxies generally suggest drier conditions and reduced rainfall across the continent

155   during this period (Wirtz et al., 2010; Prado et al., 2013), as shown in Figures 1b and 1g. A few sites in northeastern Brazil show evidence of wetter conditions (Figure 1g), likely due to enhanced regional land–sea breeze under the changes in the position and intensity of the South Atlantic subtropical high during the mid-Holocene (Nagai et al., 2009; Prado et al., 2013). In Australia, however, the known problem of spatial discrepancies between simulated precipitation changes and reconstructions still remains, as discussed by Liu et al. (2019) and Lowry and McGowan (2024) and shown in Figures 1b and 1f. For northern

160   Australia, recent studies indicate that the contraction of the local ITCZ contributed to reduced monsoon activity and precipitation (Reeves et al., 2013; Proske et al., 2014; Field et al., 2017; Lowry and McGowan, 2024), which aligns with PMIP4 simulation results (Figures 1b and 1f). Additionally, some sites of pollen reconstructions in southeastern Australia indicate increased precipitation during the mid-Holocene (Herbert and Harrison, 2016; Lowry and McGowan, 2024), while PMIP4 simulations do not consistently capture those robust changes in Figure 1b.
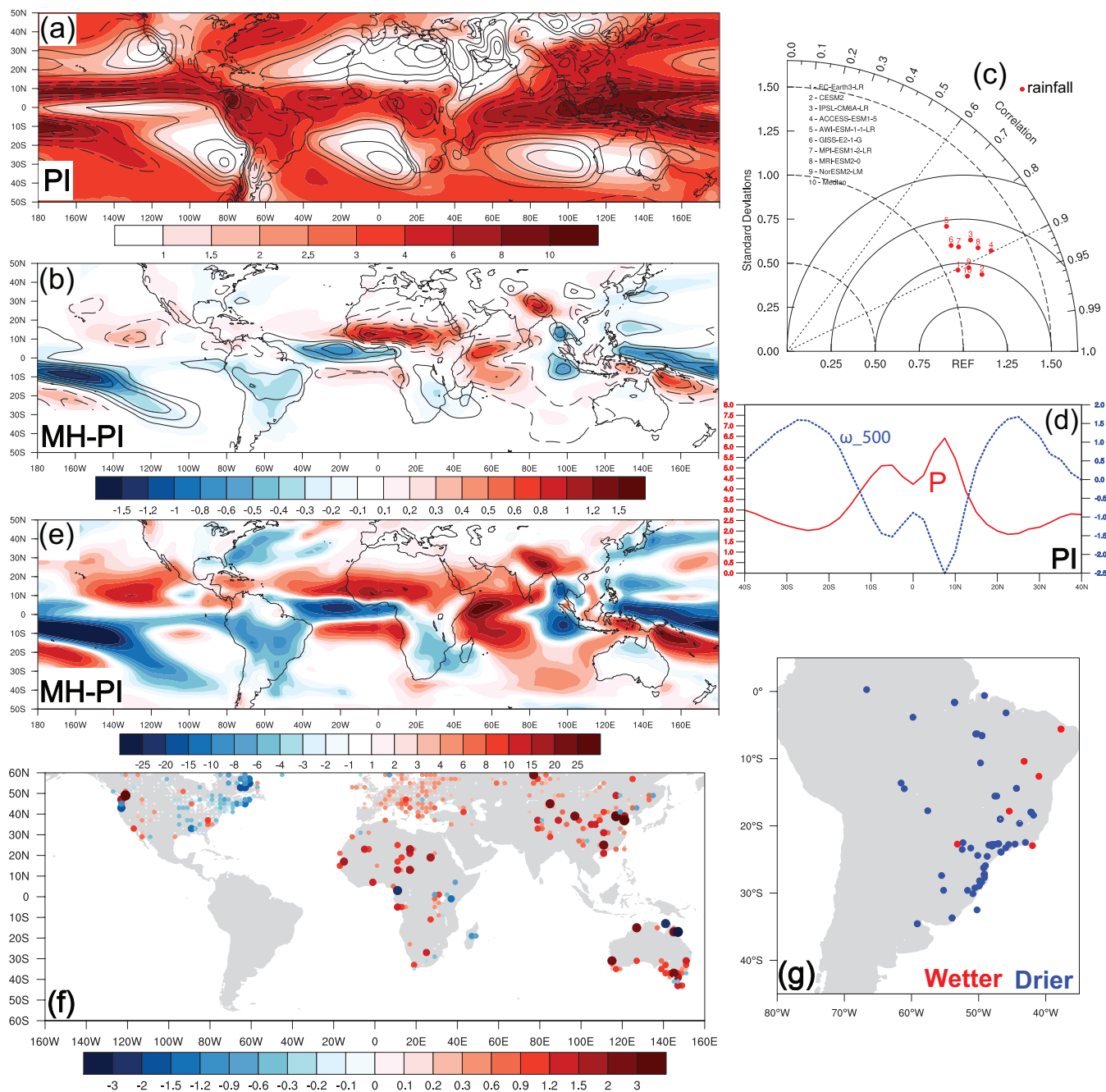
Figure 1. (a) Annual mean precipitation (colored; unit: mm/day) and ω at 500 hPa (contour) in the PI period. (b) as (a), but for the changes of annual precipitation and ω at 500 hPa from the PI to the MH period. The solid (dashed) contours indicate positive (negative) anomalies of ω at 500 hPa, with a interval of 10^{-2} and $0.2 \cdot 10^{-2} \ Pa \ s^{-1}$ in (a) and (b), respectively. (c) the Taylor diagram for the global distribution of annual mean rainfall between each model in the PI simulation and the observation (GPCP, 1979-2018, as the REF). (d) Annual and zonal mean precipitation and ω at 500 hPa during the PI period. (e) the changes of the divergence of column total energy transport (unit: $W m^{-2}$). See Eq. (6) for further details. (f) Reconstructed annual precipitation changes (unit: mm/day) from pollen proxy (Bartlein et al., 2011; Herbert and Harrison, 2016; Lowry and McGowan, 2024). Sites with red color indicate increased mid-Holocene rainfall compared to present-day (0 ka) proxy records, and blue ones for reduced rainfall. (g) Multiple types of proxies from other compilations in the South America (Wirtz et al., 2010; Prado et al., 2013).

Table 1. Mid-Holocene latitude changes in the width (°) and strength (%) of the Southern and Northern Hadley cells

Model	ΔWidth_S		ΔWidth_N		ΔStrength_S		ΔStrength_N	
	I	**II**	**I**	**II**	**I**	**II**	**I**	**II**
1	2.3	1.0	-2.3	-1.0	6.6%	4.5%	-6.9%	-6.6%
2	-0.2	0.5	0.0	-0.3	2.1%	1.2%	-0.1%	-1.4%
3	0.8	0.3	-0.5	-0.3	3.3%	1.7%	-5.2%	-5.2%
4	1.3	0.5	-1.5	-0.5	4.0%	3.3%	-3.1%	-3.6%
5	1.3	0.5	-0.8	0.0	1.2%	0.6%	-4.9%	-6.0%
6	0.5	0.3	-0.3	-0.3	1.1%	-0.2%	-4.2%	-3.9%
7	2.8	1.3	-2.0	-0.5	1.2%	0.03%	-5.5%	-5.8%
8	1.3	0.8	-1.3	-1.0	2.9%	1.6%	-2.2%	-3.6%
9	0.5	0.5	-1.0	-0.5	3.9%	3.2%	-0.8%	-1.2%
Mean	**1.2**	**0.6**	**-1.1**	**-0.5**	**2.9%**	**1.8%**	**-3.7%**	**-4.1%**

3.2 Hydrological effects of the ITCZ shift and associated Hadley cell changes

To examine the relationship between changes in the ITCZ and the Hadley cell, we use two different precipitation metrics to quantify the ITCZ location, one defined as the precipitation centroid and the other as the median latitude of precipitation between $20°S$ and $20°N$ (See Eqs. S1-S2 in the Supplementary material), and the two different streamfunction metrics defined in Section 2.2 to measure the edges, widths, and strengths of the northern and southern Hadley cells.

As shown in Table 1, the changes in width and strength are positively correlated among the models. A wider Hadley cell tends to accommodate greater total upward and downward mass fluxes, and is therefore stronger as measured by the streamfunction maximum, even if the intensity of vertical motions remains relatively stable. Compared to the PI period (Figure 2a), the northern Hadley cell becomes narrower with weaker overturning circulation, which is associated with northward shifted rising motion and reduced subsidence in the northern part of the cell as shown in Figure 2b. Specifically, the ensemble mean PMIP4 simulations indicate that the strength of the northern Hadley cell during the mid-Holocene is reduced by 3.7% and 4.1% according to the two different streamfunction metrics (Table 1). For changes in the northern Hadley cell width, the ensemble mean result shows a contraction by 1.1° and 0.5°, respectively.

Conversely, the expansion of the southern Hadley cell, as indicated by the two mass streamfunction metrics in Table 1, is accompanied by enhanced strength. This expansion suggests a stronger and northward extended overturning circulation with widespread tropospheric drying south of the equator (Figures 2b and 2d). During the mid-Holocene, the southern Hadley cell strength by ensemble mean is enhanced by 2.9% and 1.8% using the two metrics (Table 1). Additionally, the ensemble mean changes in the southern Hadley cell width show and expansion of 1.2° and 0.6° in latitude, respectively.
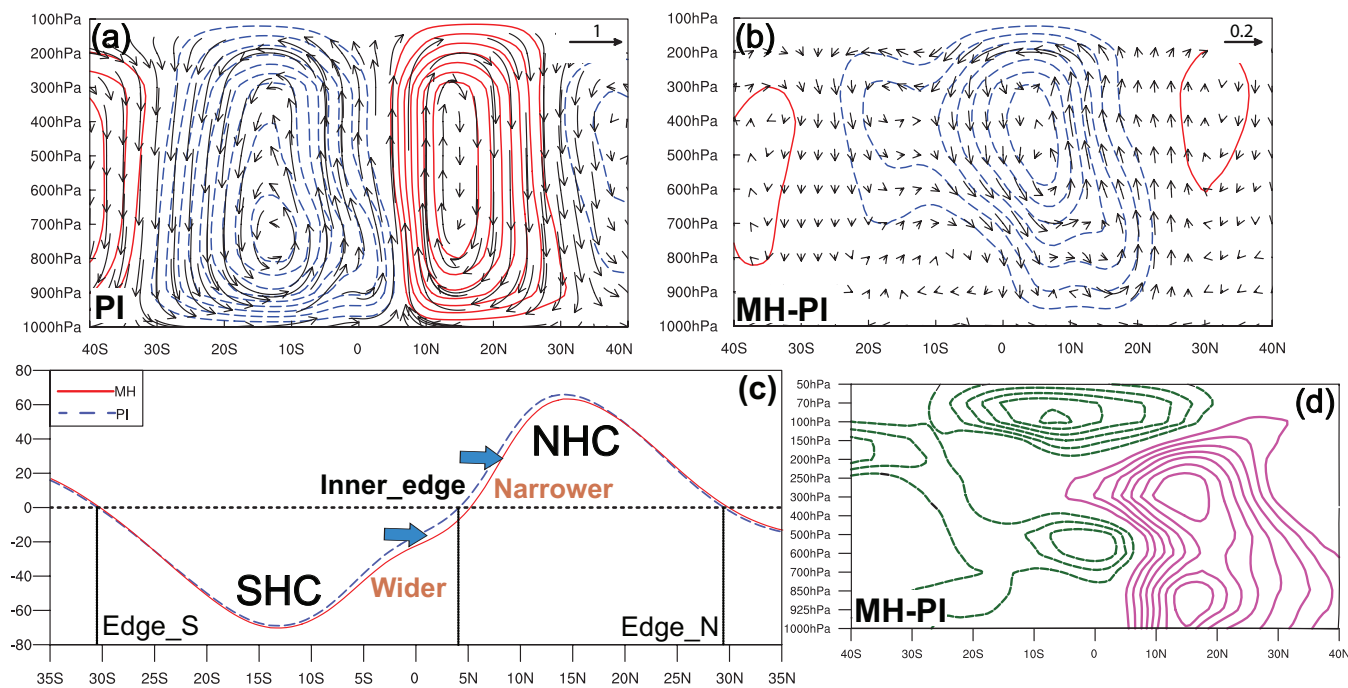
Figure 2. (a) Annual mean Hadley cell during the PI period, with solid contours representing positive values and dashed contours indicating negative values of the meridional mass streamfunction (unit: 10^{10} kg/s). Meridional circulation $(v, -\omega)$ is shown by vectors, scaled by 1 ms^{-1} and $10^{-2}\ Pa\ s^{-1}$, respectively. (b) Changes of meridional mass streamfunction in the mid-Holocene. Solid (dashed) contours have a interval of 10^9 kg/s, and the meridional circulation changes are scaled by 0.2 ms^{-1} and $0.2 \cdot 10^{-2}\ Pa\ s^{-1}$, respectively. (c) Meridional Hadley cell depicted by the zonal mean, vertically-weighted mass streamfunction between 900 and 200 hPa during the PI (blue) and the MH (red) periods (unit: 10^9 kg/s). Vertical lines in (c) indicate the northern, inner, and southern Hadley cell edges. (d) as (b), but for changes of zonal mean relative humidity. Solid (dashed) contours indicate positive (negative) anomalies (interval: 0.5%).

Our findings further suggest that these changes in the widths of the southern and northern Hadley cells are primarily driven by a northward shift of the inner edge in the mid-Holocene, as illustrated in Figure 2c. The mid-tropospheric streamfunction metric (Ψ_{500hPa}) reveals an ensemble mean northward shift of 1.4° for the Hadley cell inner edge during the mid-Holocene, which is larger than the shift based on the vertically weighted streamfunction metric ($\langle\Psi\rangle_{900-200hPa}$) by 0.7° (Figures 3a, 3b). The intermodel standard deviations (STD) for the change in the Hadley cell inner edge shift is 0.8° for the Ψ_{500hPa} metric, and 0.3° for the $\langle\Psi\rangle_{900-200hPa}$ metric. Both STDs are smaller than the multi-model mean changes, with closer agreement observed for the Hadley cell inner edge changes when using the $\langle\Psi\rangle_{900-200hPa}$ metric (Figures 3a and 3b).

The mid-Holocene shifts in the global and annual ITCZ positions, derived from the first and second precipitation metrics, reveal an average northward migration of 0.2° and 0.3°, respectively (Figures 3c and 3d). These findings align closely with multiple mid-Holocene proxy records, which suggest a northward ITCZ migration of the ITCZ up to 1° (Haug et al., 2001; McGee et al., 2014). Furthermore, the STDs of the ITCZ location change by the first and second metrics are 0.1° and 0.2°,
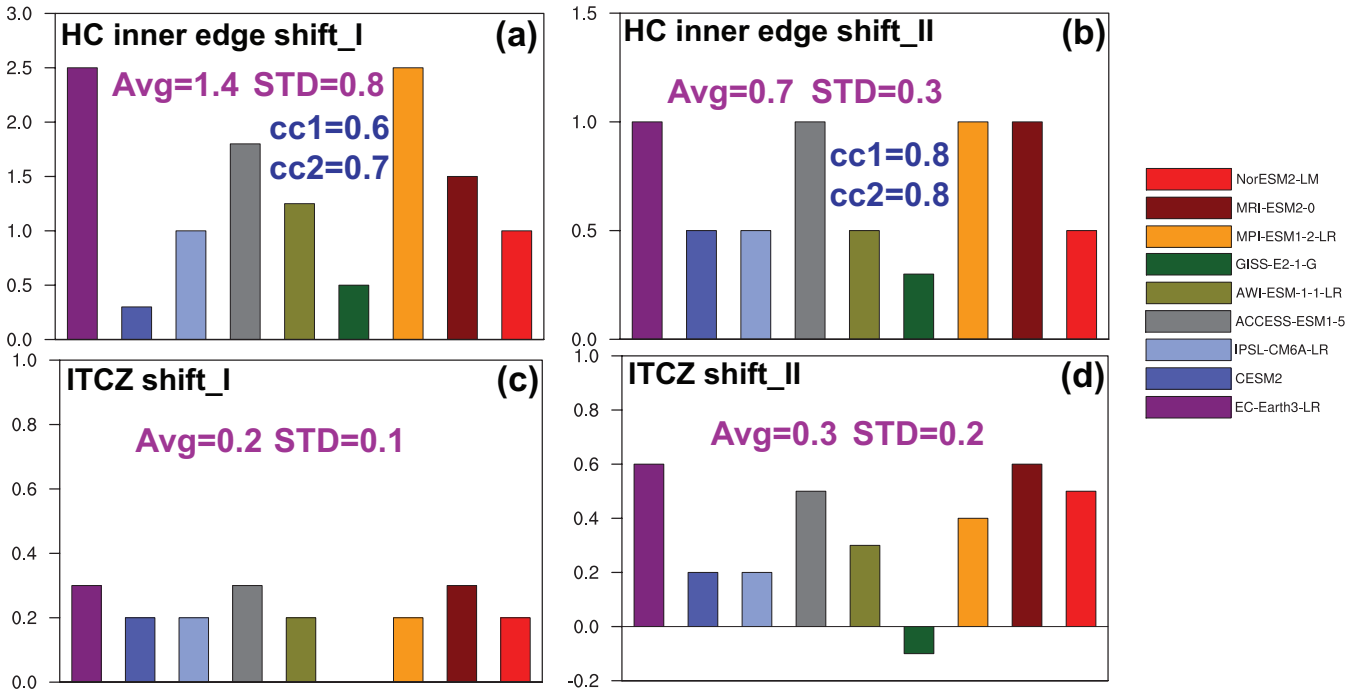
Figure 3. (a) and (b) are the latitude changes ($^{\circ}N$) of Hadley cell inner edge using the two streamfunction metrics, respectively. (c) and (d) are the latitude changes ($^{\circ}N$) of ITCZ position using the two precipitation metrics, respectively. Note the change of GISS-E2-1-G in (c) is zero. $cc1$ and $cc2$ in (a) denote the intermodel correlation coefficients between the shifts in the Hadley cell inner edge using the first streamfunction metric and the shifts in the ITCZ position by the two precipitation metrics, respectively. $cc1$ and $cc2$ in (b) are as in (a), but for the shifts of Hadley cell inner edge using the second streamfunction metric.

respectively, as shown in Figures 3c and 3d. The first (precipitation centroid) metric thus exhibits a better agreement among

195   models with a smaller STD.

Previous studies of global warming reveal that the northward ITCZ migration tends to position the Hadley cell outer edge more poleward and influence Hadley cell width (Kang and Lu, 2012; Lau and Kim, 2015; Watt-Meyer and Frierson, 2019; Lionello et al., 2024). Our results indicate that the northward movement of its inner edge could also contribute to changes in the Hadley cell width during the mid-Holocene. Figures 3a and 3b show a strong positive correlation between shifts in

200   the global ITCZ location and the inner boundary of the Hadley cell during the mid-Holocene across all the metrics used in this study. For the Ψ_{500hPa} metric to define the Hadley cell inner edge shift, its correlation with the two precipitation-based metric of ITCZ location shift is 0.6 and 0.7 (Figure 3a). The corresponding correlation when basing the Hadley cell shift on the $\langle\Psi\rangle_{900-200hPa}$ metric is slightly higher at 0.8 for both two precipitation metrics (Figure 3b).

Understanding changes in the Hadley cell and ITCZ is crucial for comprehending how alterations in large-scale circulations

205   further affect the global hydrological cycle during the mid-Holocene. To investigate this, we conduct the moisture budget

analysis by using mass-weighted vertical integration

$$\delta\overline{P} = \delta\overline{E} \underbrace{-\langle\overline{\mathbf{V}}\cdot\nabla_p\delta\overline{q}\rangle - \langle\delta\overline{q}\nabla_p\cdot\overline{\mathbf{V}}\rangle}_{\delta TH} \underbrace{-\langle\delta\overline{\mathbf{V}}\cdot\nabla_p\overline{q}\rangle - \langle\overline{q}\nabla_p\cdot\delta\overline{\mathbf{V}}\rangle}_{\delta DY} \underbrace{-\langle\nabla_p\cdot\delta(\overline{\mathbf{V}'q'})\rangle}_{\delta TE} + \delta S \tag{9}$$

where $\delta(\cdot)$ denotes $(\cdot)_{MH} - (\cdot)_{PI}$. $\overline{P}$ is the annual precipitation, $\overline{q}$ is specific humidity, $\overline{E}$ is the evaporation, $\mathbf{V}$ is the horizontal wind. The vertical integration $\langle\cdot\rangle$ is from 1000 to 100 hPa. Eq. (9) further decomposes the precipitation change

210 to contributions from five RHS terms, including the evaporation term ($\delta\overline{E}$), thermodynamic term (δTH), the dynamic term (δDY), the transient eddy flux term (δTE), and the surface term (δS). Furthermore, δS and δTE are approximately derived as: $\delta S \approx -\delta(\nabla_p\cdot\langle\overline{\mathbf{V}q}\rangle) - \delta TH - \delta DY$, and $\delta TE \approx \delta\overline{P} - \delta\overline{E} + \delta(\nabla_p\cdot\langle\overline{\mathbf{V}q}\rangle)$, following Seager and Henderson (2013).

During the mid-Holocene, there is a reduction in moisture convergence in the tropics, as shown by the negative $\overline{P} - \overline{E}$ anomalies in Figure 4a, while the subtropics show a wetting trend, particularly in the Northern Hemisphere's subtropical

215 regions, accompanied by positive $\overline{P} - \overline{E}$ anomalies. The comparison between continents and oceans shows that the northward shift in annual rainfall associated with the ITCZ and Hadley cell predominantly occurs over land (Bian and Räisänen, 2024), as shown in Figures 4c and 4e. Specifically, the transient eddy flux term in Eq. (9) emerges as the leading contribution to the increase in terrestrial precipitation in the Northern Hemisphere (Bian and Räisänen, 2024), with evaporation playing a secondary role, and dynamic and thermodynamic terms have a comparatively smaller influence (Figure 4c). Additionally, for

220 the reduced precipitation in the Southern Hemisphere, the evaporation and dynamic terms play a primary role.

In summary, the northward ITCZ migration leads to a contracted and weakened northern Hadley cell in the mid-Holocene, accompanied by a weaker overturning circulation and reduced subtropical descending branch, leading to stronger rising motion, wetter tropospheric conditions, and increased terrestrial precipitation within the northern Hadley cell region. By contrast, the southern Hadley cell expands and intensifies during this period, accompanied by enhanced overturning circulation and

225 strengthened subtropical descending branch. This leads to drier tropospheric conditions, and decreased terrestrial precipitation within the southern Hadley cell region.

3.3 Physical mechanisms driving terrestrial hydrological changes

The northward ITCZ migration and associated Hadley cell changes can further lead to shifts in terrestrial hydroclimates (Diaz and Bradley, 2004; Hill et al., 2017; Hill, 2019; Lionello et al., 2024). To explore these changes, we further investigate the

230 energy constraints influencing the terrestrial hydrological cycle during this period.

Consistent with the discussion in Section 3.1, Figures 4c, 4d, and 4f further illustrate that the increased terrestrial rainfall is closely linked to positive anomalies in atmospheric energy divergence ($\nabla\cdot\overline{\mathbf{F}_a} > 0$) over the Northern Hemisphere. This is primarily driven by enhanced vertical moist static energy (MSE) advection over land (Terms III and IV), while changes in horizontal MSE advection (Terms I and II) and eddy MSE flux (Term V) have a compensating influence, as illustrated in Figure

235 4f.

For the $\delta\nabla\cdot\overline{\mathbf{F}_a} > 0$ and associated changes in MSE advection, two physical pathways are relevant. First, changes in radiative forcing due to orbital parameters result in increased net radiation ($\delta\overline{R_a} > 0$) in the Northern Hemisphere (Figures 4b, 4d),

altering the energy balance of the atmosphere ($\delta \nabla \cdot \overline{\mathbf{F}_a}$). This further influences the temperature and moisture distributions and affects the MSE gradient and advection over land during the mid-Holocene. Second, strong positive latent heating anomalies

240   over land significantly contribute to enhance vertical MSE advection (Figures 4d, 4f). As moist air from the lower levels rises and cools, the latent heat released by the condensation increases the buoyancy of the air parcel, promoting atmospheric instability and stronger updrafts, which facilitate the development of convective systems (Hill et al., 2017; Adames and Maloney, 2021). Additionally, Figure 4c shows enhanced moisture convergence anomalies, combined with increased vertical MSE advection (Figure 4f), resulting in enhanced terrestrial moist convection and precipitation in the Northern Hemisphere during this

245   period. In contrast, reduced rising motion in the Southern Hemisphere causes negative anomalies in vertical MSE advection, suppressing moist convection and precipitation during the mid-Holocene.

Figure 4f further shows that enhanced vertical MSE advection over land is primarily due to stronger rising motion (Term IV) within the northern Hadley cell region (Figure 2b). Changes in the vertical MSE gradient profile (Term III in Eq. (6)), play a secondary role in promoting vertical MSE advection (Figure 4g). Furthermore, the spatial distributions of Terms III and IV

250   further indicate that positive anomalies in vertical MSE advection are predominantly concentrated in monsoonal regions of the Northern Hemisphere, playing a key role in promoting terrestrial moist convection and increasing monsoonal rainfall, as illustrated in Figures 4g and 4h.

In summary, positive anomalies in vertical MSE advection over land due to stronger upward motion create favorable conditions for moist convection and precipitation (Back and Bretherton, 2006; Chou et al., 2013; Hill et al., 2017; Hill, 2019;

255   Geen et al., 2020; Bombardi and Boos, 2021), particularly evident in the Northern Hemisphere tropics and adjacent subtropical regions of during the mid-Holocene.
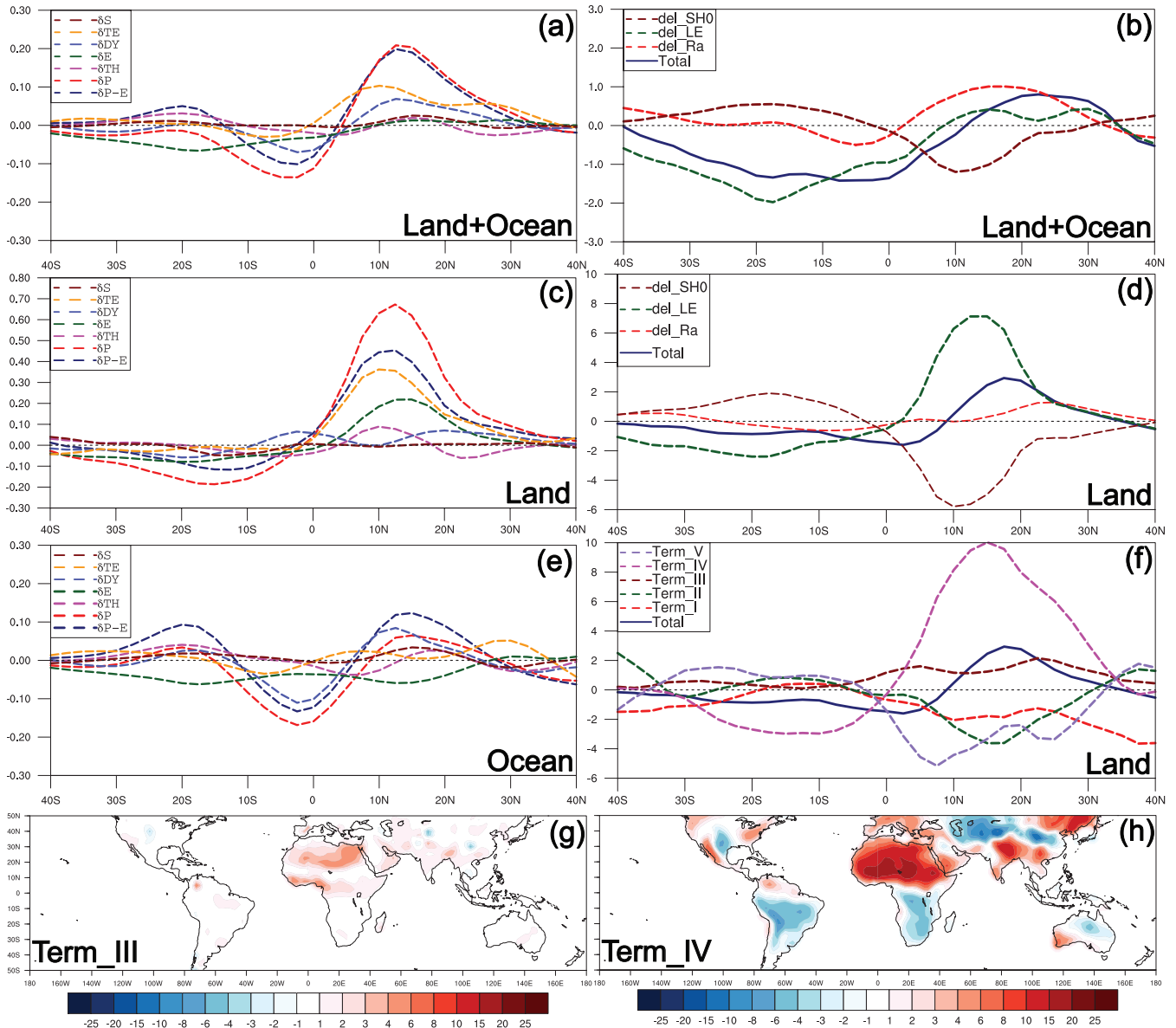
Figure 4. (a) Changes of annual and zonal mean moisture budget (Eq. (9); unit: mm/day). (c) and (e) are the changes in the moisture budget over land and ocean, respectively (unit: mm/day). (b) Changes in the column energy balance (unit: Wm^{-2}). (d), (f) are as (b), but for changes of column energy balance and associated RHS terms over land (unit: Wm^{-2}), respectively. See Eqs. (6)-(8) for further details. (g) and (h) show the distribution of the RHS terms III and IV in Eq. (6) over land, respectively.

3.4 Impact of hydrological changes on land aridity

The northward ITCZ migration and associated Hadley cell changes can further lead to shifts in regional climates, altering terrestrial dryness across the tropics and subtropics and resulting in changes to regional drylands during the mid-Holocene
260 (Diaz and Bradley, 2004; Lu et al., 2007; Lau and Kim, 2015; Liu et al., 2019; Lionello et al., 2024). We further assess the influence of terrestrial hydrological changes on land aridity during the mid-Holocene by analyzing the climatological moisture availability index (alpha), aridity index (AI), and runoff ratio.

The alpha index is defined as the ratio of annual evaporation to annual potential evaporation (PET), and the runoff ratio is defined as the proportion of annual runoff to annual precipitation. The commonly used AI is defined as the ratio of annual PET
265 to annual precipitation, typically calculated using the Penman-Monteith (PM_AI) reference model for PET (Allen et al., 1998; Feng and Fu, 2013). However, recent studies have shown limitations with the PM_AI method for calculating PET, noting that it can significantly overestimate projected aridity changes (Greve et al., 2019; Yang and Roderick, 2019). Milly and Dunne (2016) found that the PM_AI based method often overpredicts changes in evaporation over well-watered surfaces in climate models. In this study, we employ a net surface radiation (R_s) based method for calculating PET, using estimates of R_s as the energy
270 constraint on evaporation (Milly and Dunne, 2016; Yang and Roderick, 2019; Yang et al., 2019; Greve et al., 2019). Although this is a simplified approach to estimate PET, there is a reasonable empirical correspondence between PET and net surface radiation (Milly and Dunne, 2016; Greve et al., 2019), as $PET = 0.8\frac{R_s}{L}$, where L represents the latent heat of vaporization.

To quantify the influence of precipitation, evaporation, and PET on land aridity changes, we decompose the AI and runoff ratio index changes by Taylor expansion:

275
$$\delta(\text{AI}) = \delta\left(\frac{\overline{PET}}{\overline{P}}\right) = \frac{1}{\overline{P}}\delta\overline{PET} - \frac{\overline{PET}}{\overline{P}^2}\delta\overline{P} + Ro_1 \tag{10}$$

and

$$\delta(\text{runoff ratio}) = \delta\left(\frac{\overline{P} - \overline{E}}{\overline{P}}\right) = -\frac{1}{\overline{P}}\delta\overline{E} + \frac{\overline{E}}{\overline{P}^2}\delta\overline{P} + Ro_2 \tag{11}$$

where $\delta(\cdot)$ denotes $(\cdot)_{MH} - (\cdot)_{PI}$.

$\frac{1}{\overline{P}}\delta\overline{PET}$ is the contribution of PET changes to AI changes, and $-\frac{\overline{PET}}{\overline{P}^2}\delta\overline{P}$ is the contribution of precipitation changes
280 to AI changes. $-\frac{1}{\overline{P}}\delta\overline{E}$ is the contribution of evaporation changes to runoff ratio changes, and $\frac{\overline{E}}{\overline{P}^2}\delta\overline{P}$ is the contribution of precipitation changes to runoff ratio changes. Ro_1 and Ro_2 are the residual terms representing non-linear effects (not discussed in this study).
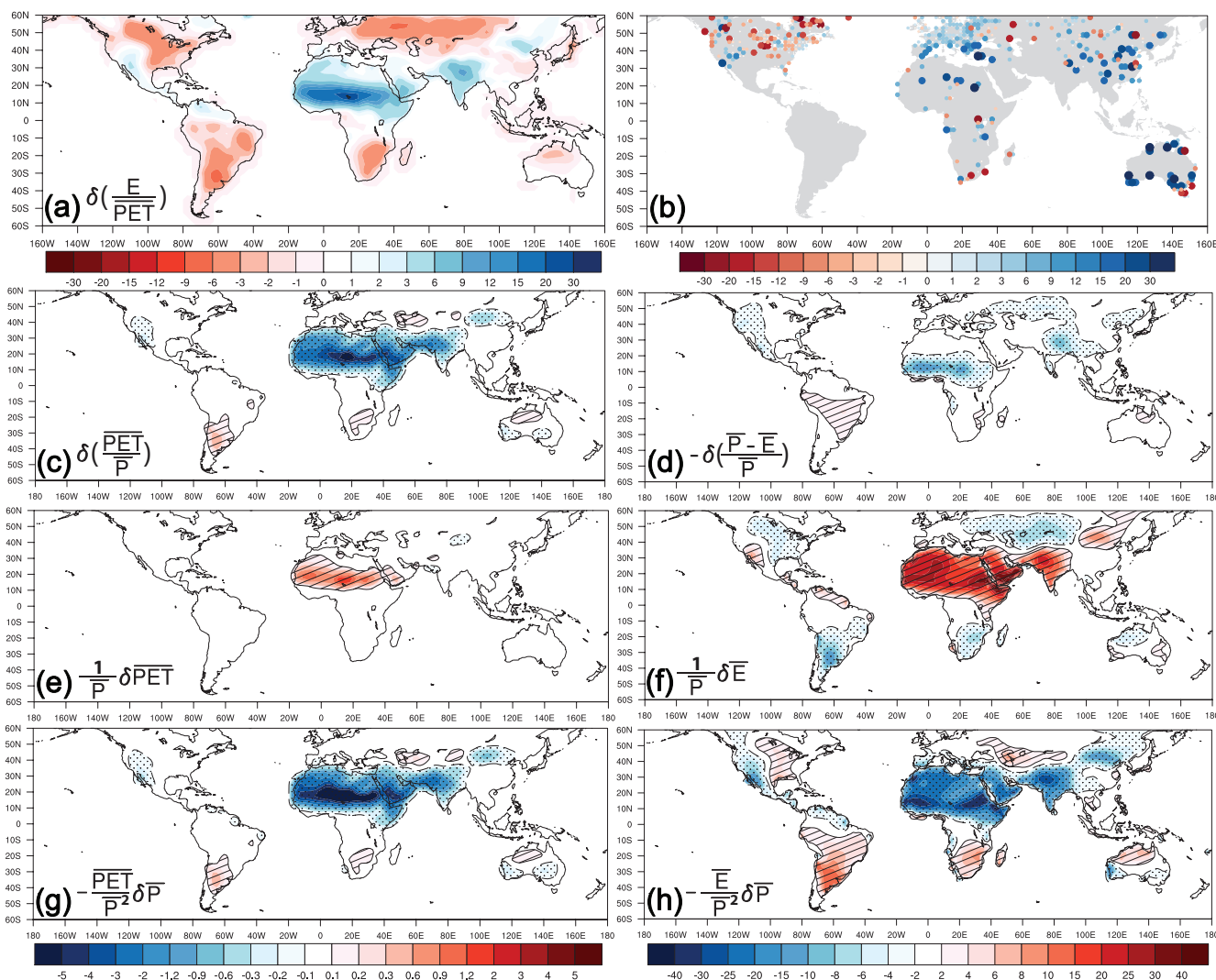
Figure 5. (a) Changes (%) of moisture availability index (alpha) as the ratio of annual evaporation to PET. (b) Reconstructed alpha changes (%) from pollen proxy (Bartlein et al., 2011; Herbert and Harrison, 2016; Lowry and McGowan, 2024). Sites with blue color indicate wetter soil conditions during the mid-Holocene compared to present-day (0 ka) proxy records, and red ones for drier soil conditions. (c) Changes of annual AI. (d) as (c), but for the reversed changes (%) of annual runoff ratio from the PI to the MH period. (e), (g) are the first and second RHS terms of Eq. (10) for AI changes. (f) and (h) are the contributions of the first and second RHS terms in Eq. (11) to the runoff ratio changes (%), with signs reversed.

The reconstructed precipitation changes are closely linked to changes in the reconstructed moisture availability index (alpha) based on pollen records from the mid-Holocene (Bartlein et al., 2011; Herbert and Harrison, 2016; Lowry and McGowan, 2024), as shown in Figures 1f and 5b. Furthermore, the comparison of the spatial distribution of changes in the simulated alpha index (Figure 5a), AI (Figure 5c), and runoff ratio (Figure 5d) generally indicates that monsoonal regions experience wetter conditions with reduced terrestrial aridity in the Northern Hemisphere, leading to a contraction of regional drylands during the mid-Holocene (Figures 6a-6d). Additionally, despite simulated circulation changes that generally favor increased moist convection and rainfall in the Northern Hemisphere, pollen records in eastern North America and central Asia indicate a drier climate than at present (Bartlein et al., 2011). Analysis of the RHS terms in Eqs. (10) and (11) suggests that increased precipitation is the primary factor driving wetter conditions and the reduction of terrestrial aridity in the Northern Hemisphere (Figures 5g, 5h), while changes in PET and evaporation have a compensatory effect (Figures 5e, 5f). Specifically, changes in evaporation contribute to drier conditions in eastern North America and central Asia, as reflected in the alpha index changes shown by pollen records in Figure 5b, while changes in AI and runoff ratio fail to capture these regional transitions to drier climate.

In the Southern Hemisphere, both simulations and reconstructions indicate a generally drier climate during the mid-Holocene (Bartlein et al., 2011; Prado et al., 2013; Herbert and Harrison, 2016; Lim et al., 2016; Liu et al., 2019; Lowry and McGowan, 2024), resulting in increased terrestrial aridity and the expansion of regional drylands in South America, southeastern Africa, and northern Australia (Figures 5c-5d, 6e-6g). However, simulated land dryness changes in Australia, represented by the alpha index (Figure 5a), AI (Figure 5c), and runoff ratio (Figure 5d), still show spatial discrepancies when compared to reconstructions in Figure 5b, as noted earlier by Liu et al. (2019) and Lowry and McGowan (2024). While PMIP4 simulation results in Figure 1b indicate drier conditions in northern Australia, only a few pollen records near the Cape York Peninsula and northeastern Australia support this shift while others do not (Lowry and McGowan, 2024). Additional reconstructions from northwestern Australia reveal reduced fluvial activity and dune reactivation (Reeves et al., 2013), and a reduction in rain-forest taxa and mangrove (Proske et al., 2014; Field et al., 2017), indicating a contraction of the local ITCZ that contributes to reduced Australian monsoon activity and precipitation (Reeves et al., 2013). Furthermore, part of pollen records from southeastern Australia (Figure 5b) indicate wetter conditions during the mid-Holocene (Herbert and Harrison, 2016; Lowry and McGowan, 2024), which are likely caused by precipitation-driven reduced terrestrial aridity shown in AI and runoff ratio changes (Figures 5g, 5h, 6g). However, as discussed in Section 3.1, the PMIP4 simulations do not consistently capture these significant precipitation changes in reconstructions (Figure 1f).
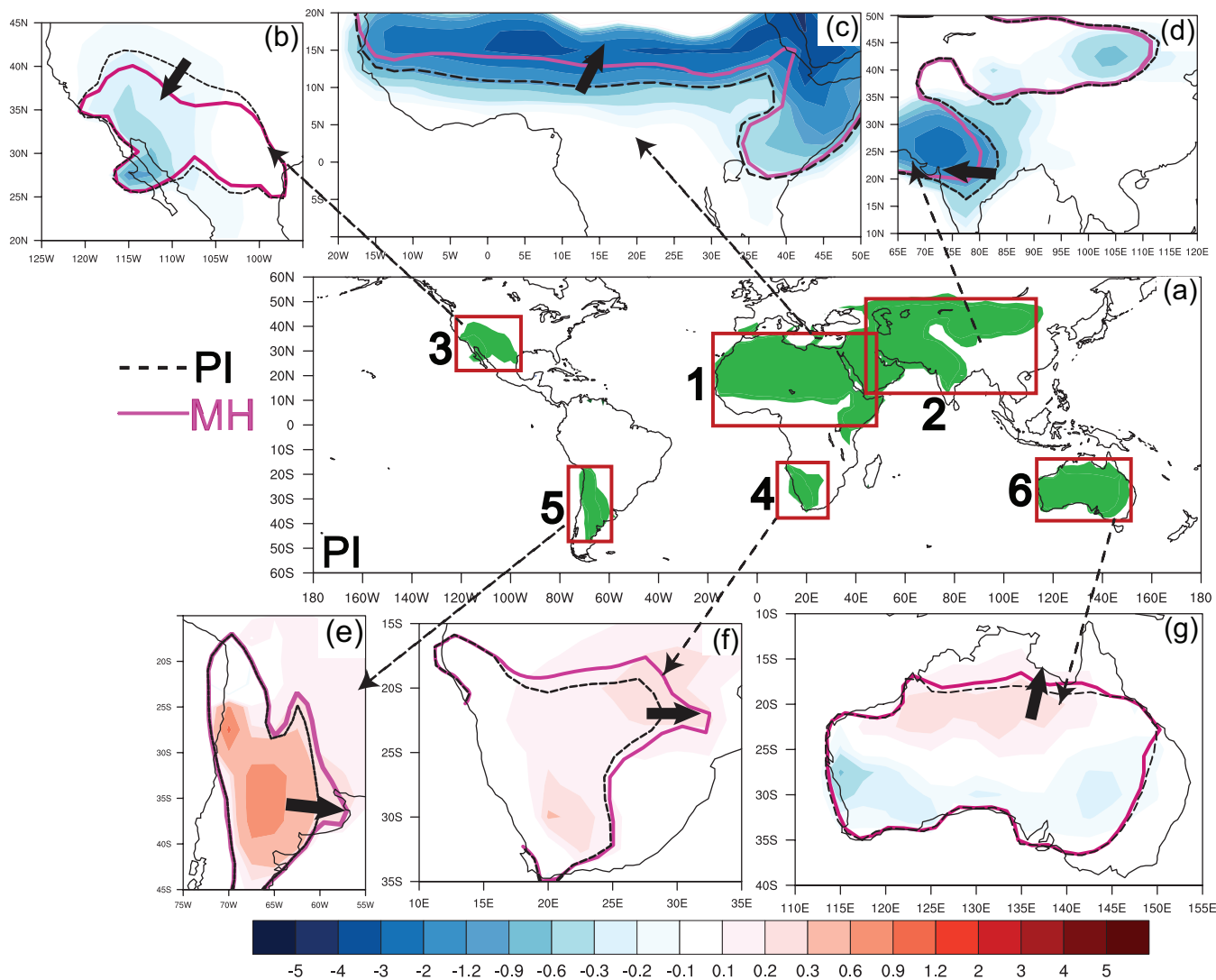
Figure 6. (a) Annual mean dryland distribution by aridity index (AI) in the PI period. The shaded areas denote drylands (semi-desert and desert) with AI values equal and larger than 1.6, adapted from Nicholson (2011). (c)-(g) are dryland shifts between the PI and MH periods. The colored values in (c)-(g) denote AI anomalies.

4 Summary and discussion

This study investigates the impacts of northward ITCZ migration on multiple Hadley cell characteristics and their combined influence on the global hydrological cycle and terrestrial aridity during the mid-Holocene, approximately 6,000 years ago. Known as the "Green Sahara", this era was marked by significant climatic changes, with arid regions like the Sahara expe-
315 riencing wetter conditions. We apply different precipitation metrics to quantify the global ITCZ position, and the widths and strengths of the Hadley cell are based on two mass streamfunction metrics, using nine simulations from the PMIP4-CMIP6 archive.

Our findings indicate that during the mid-Holocene, increased solar radiation in the Northern Hemisphere, driven by orbital forcing, shifted the ITCZ northward by 0.2° and 0.3° using two different metrics. Those shifts align with mid-Holocene proxy
320 evidence indicating a northward ITCZ migration up to 1° (Haug et al., 2001; McGee et al., 2014). The northward ITCZ migration leads to multiple changes in the Hadley cell that differ from those changes under the current greenhouse gas (GHG)-induced warming climate (Lu et al., 2007; Lau and Kim, 2015; Byrne et al., 2018; Grise and Davis, 2020; Pikovnik et al., 2022; Lionello et al., 2024; Wu et al., 2024). Specifically, the northern Hadley cell width contracted by 1.1° and 0.5° using the two metrics, and its strength reduced by 3.7% and 4.1%, with weaker overturning circulation, stronger rising motion, and a
325 wetter troposphere during the mid-Holocene. This contributes to increased precipitation in the tropics and adjacent subtropical regions, particularly in monsoonal regions of the Northern Hemisphere. Conversely, the southern Hadley cell expanded by 1.2° and 0.6° and strengthened by 2.9% and 1.8%, with stronger overturning circulation, reduced rising motion near and to the south of the Equator, and a drier troposphere, contributing to decreased precipitation in the Southern Hemisphere. Under the current GHG-induced warming scenario, the ITCZ narrows and intensifies, leading to the "deep-tropics squeeze" (DTS) phenomenon
330 and affecting the Hadley cell by concentrating rising air, strengthening meridional circulation, and causing drier subtropical conditions with expanding drylands (Lu et al., 2007; Lau and Kim, 2015; Lionello et al., 2024). These differences highlight the distinct impacts of orbital forcing and GHG-induced warming on large-scale circulation dynamics and hydrological patterns.

Moisture budget analysis reveals that mid-Holocene precipitation changes are driven by variations in key components: evaporation, moisture advection, and eddy fluxes. Enhanced eddy fluxes significantly contribute to increased terrestrial precipitation
335 across the Northern Hemisphere tropics and adjacent subtropical regions. In contrast, negative Southern Hemispheric precipitation anomalies are primarily attributed to evaporation and dynamic factors. Furthermore, increased radiative heating and terrestrial latent heating in the Northern Hemisphere alter the MSE gradient and advection, intensifying moist convection and precipitation. Specifically, enhanced rising motion leads to positive anomalies in vertical MSE advection over land, further promoting moist convection and precipitation in the Northern Hemisphere. Conversely, weaker rising motion leads to reduced
340 vertical MSE advection in the Southern Hemisphere, suppressing moist convection and precipitation.

The northward ITCZ migration and the associated changes in Hadley cell significantly influence regional climates by altering terrestrial dryness across the tropics and subtropics. Both simulations and reconstructions generally agree on the wetter conditions in the Northern Hemisphere (Bartlein et al., 2011), supporting the conclusion of a northward-shifted ITCZ and a narrowed, weakened northern Hadley Cell. These changes contribute to reduced land aridity in tropical and adjacent subtrop-

345 ical regions of the Northern Hemisphere. Additionally, pollen records and other types of proxies generally indicate a drier climate in the Southern Hemisphere, consistent with the simulated expansion of the southern Hadley cell and reduced moisture convergence. However, notable discrepancies remain between simulations and reconstructions in some regions, particularly in Australia (Liu et al., 2019; Lowry and McGowan, 2024).

As the alpha index used in simulations and reconstructions can be influenced by variations in temperature and evaporation, 350 its changes are generally less consistent and pronounced than those observed in precipitation. The temperature-related changes in evaporation may cause significant changes in the alpha index even in areas with minimal changes in precipitation. Therefore, potential uncertainties in the pollen-based reconstructed alpha index should also be considered (Bartlein et al., 2011). Other potential biases in quantitative climate reconstructions based on pollen data include the impact of local vegetation on the pollen assemblages, differences in pollen productivity and dispersal, and the lack of suitable sedimentary environments, notable lakes, 355 in the arid regions in tropics and subtropics (Birks et al., 2011; Huntley, 2012). Additionally, another source of uncertainty is the extent to which changes in the AI effectively impact soil moisture and land aridity (Greve et al., 2019; Scheff et al., 2021, 2022). This highlights the importance of comparing changes in the alpha index, AI, and runoff ratio to assess land aridity changes during the mid-Holocene. Recognizing inherent uncertainties in both climate simulations and reconstructions is essential.

Furthermore, the PMIP4 simulations do not account for the dynamic feedbacks caused by the climate-vegetation coupling 360 and emissions of multiple types of aerosols, leaving uncertainty about how a fully coupled atmosphere-ocean-vegetation-aerosol framework might influence the simulated global hydrological cycle and terrestrial aridity during the mid-Holocene (Pausata et al., 2016; Tierney et al., 2017; Hopcroft and Valdes, 2019; Brierley et al., 2020; Pausata et al., 2020; Bian et al., 2023; Jungandreas et al., 2023). In the "Green Sahara" period, multiple reconstructions have shown significantly increased precipitation, amplified vegetation cover, and reduced dust emissions (Claussen et al., 2017; Tierney et al., 2017; Pausata 365 et al., 2020; Brierley et al., 2020; Thompson et al., 2022; Kaufman and Broadman, 2023). These findings highlight the critical role of vegetation and aerosols feedbacks in shaping mid-Holocene climate. Therefore, exploring how global-scale changes in dynamic vegetation cover and aerosol emissions interact to modulate ITCZ migration, Hadley Cell adjustments, and the evolution of the global hydrological cycle is crucial for future mid-Holocene study.

Overall, this study underscores the complex interactions among orbital forcing, the ITCZ, the Hadley cell, global hydrologi-370 cal cycle, and terrestrial aridity during the mid-Holocene. While climate models provide valuable insights into these dynamics, it is crucial to acknowledge their limitations and the uncertainties associated with both simulations and reconstructions. Continued research and model development are needed to improve our understanding of past climate changes and their implications for the future.

Data availability. The PMIP4-CMIP6 simulations are available at https://esgf-node.llnl.gov/. The GPCP monthly precipitation dataset is available at https://downloads.psl.noaa.gov/Datasets/gpcp.

For alpha index and MAP pollen proxy databases in Bartlein et al. (2011), the available links are https://www.ncei.noaa.gov/pub/data/paleo/pollen/recons/bartlein2010/alpha_delta_06ka_ALL_grid_2x2.nc and https://www.ncei.noaa.gov/pub/data/paleo/pollen/recons/bartlein2010/map_delta_06ka_ALL_grid_2x2.nc. Pollen dataset for alpha index and MAP in Australia (Herbert and Harrison, 2016; Lowry and McGowan, 2024) are detailed in Tables S2 and S3 of the Supplementary material. Dataset for multiple types of proxy in South America (Prado et al., 2013) is available at https://doi.org/10.1594/PANGAEA.820035

Author contributions. J.B. conceived the study and wrote the manuscript. All authors participated in the manuscript's discussion and revision.

Competing interests. The authors declare no competing interests

Acknowledgements. J.B. is supported by the Flagship grant (337549) from the Academy of Finland. Computing resources for this research were provided by CSC - IT Center for Science.

385 **References**

Adam, O., Bischoff, T., and Schneider, T.: Seasonal and interannual variations of the energy flux equator and ITCZ. Part I: Zonally averaged ITCZ position, Journal of Climate, 29, 3219–3230, 2016.

Adames, A. F. and Maloney, E. D.: Moisture mode theory's contribution to advances in our understanding of the Madden-Julian oscillation and other tropical disturbances, Current Climate Change Reports, 7, 72–85, 2021.

390 Adler, R. F., Huffman, G. J., Chang, A., Ferraro, R., Xie, P.-P., Janowiak, J., Rudolf, B., Schneider, U., Curtis, S., Bolvin, D., et al.: The version-2 global precipitation climatology project (GPCP) monthly precipitation analysis (1979–present), Journal of hydrometeorology, 4, 1147–1167, 2003.

Allen, R. G., Pereira, L. S., Raes, D., Smith, M., et al.: Crop evapotranspiration-Guidelines for computing crop water requirements-FAO Irrigation and drainage paper 56, Fao, Rome, 300, D05 109, 1998.

395 Back, L. and Bretherton, C.: Geographic variability in the export of moist static energy and vertical motion profiles in the tropical Pacific, Geophysical research letters, 33, 2006.

Bartlein, P. J., Harrison, S., Brewer, S., Connor, S., Davis, B., Gajewski, K., Guiot, J., Harrison-Prentice, T., Henderson, A., Peyron, O., et al.: Pollen-based continental climate reconstructions at 6 and 21 ka: a global synthesis, Climate Dynamics, 37, 775–802, 2011.

Bian, J. and Räisänen, J.: Mid-holocene changes in the global ITCZ: meridional structure and land–sea rainfall differences, Climate Dynam-
400 ics, pp. 1–19, 2024.

Bian, J., Räisänen, J., and Zhang, Q.: Mechanisms for African easterly wave changes in simulations of the mid-Holocene, Climate Dynamics, 61, 3165–3178, 2023.

Birks, H. J. B., Heiri, O., Seppä, H., and Bjune, A. E.: Strengths and weaknesses of quantitative climate reconstructions based on late-Quaternary biological proxies, Open Ecology Journal, 3, 68–110, 2011.

405 Bombardi, R. J. and Boos, W. R.: Explaining globally inhomogeneous future changes in monsoons using simple moist energy diagnostics, Journal of Climate, 34, 8615–8634, 2021.

Brierley, C. M., Zhao, A., Harrison, S. P., Braconnot, P., Williams, C. J., Thornalley, D. J., Shi, X., Peterschmitt, J.-Y., Ohgaito, R., Kaufman, D. S., et al.: Large-scale features and evaluation of the PMIP4-CMIP6< i> midHolocene</i> simulations, Climate of the Past, 16, 1847–1872, 2020.

410 Byrne, M. P., Pendergrass, A. G., Rapp, A. D., and Wodzicki, K. R.: Response of the intertropical convergence zone to climate change: Location, width, and strength, Current Climate Change Reports, 4, 355–370, 2018.

Chou, C., Wu, T.-C., and Tan, P.-H.: Changes in gross moist stability in the tropics under global warming, Climate dynamics, 41, 2481–2496, 2013.

Claussen, M. and Gayler, V.: The greening of the Sahara during the mid-Holocene: results of an interactive atmosphere-biome model, Global
415 Ecology and Biogeography Letters, pp. 369–377, 1997.

Claussen, M., Kubatzki, C., Brovkin, V., Ganopolski, A., Hoelzmann, P., and Pachur, H.-J.: Simulation of an abrupt change in Saharan vegetation in the mid-Holocene, Geophysical research letters, 26, 2037–2040, 1999.

Claussen, M., Dallmeyer, A., and Bader, J.: Theory and modeling of the African humid period and the green Sahara, in: Oxford research encyclopedia of climate science, Oxford University Press, 2017.

420 Diaz, H. F. and Bradley, R. S.: The Hadley circulation: Present, past, and future: An introduction, in: The Hadley circulation: present, past and future, pp. 1–5, Springer, 2004.

Eyring, V., Bony, S., Meehl, G. A., Senior, C. A., Stevens, B., Stouffer, R. J., and Taylor, K. E.: Overview of the Coupled Model Intercomparison Project Phase 6 (CMIP6) experimental design and organization, Geoscientific Model Development, 9, 1937–1958, 2016.

Feng, S. and Fu, Q.: Expansion of global drylands under a warming climate, Atmospheric Chemistry and Physics, 13, 10 081–10 094, 2013.

425 Field, E., McGowan, H. A., Moss, P. T., and Marx, S. K.: A late Quaternary record of monsoon variability in the northwest Kimberley, Australia, Quaternary International, 449, 119–135, 2017.

Geen, R., Bordoni, S., Battisti, D. S., and Hui, K.: Monsoons, ITCZs, and the concept of the global monsoon, Reviews of Geophysics, 58, e2020RG000 700, 2020.

Greve, P., Roderick, M., Ukkola, A., and Wada, Y.: The aridity index under global warming, Environmental Research Letters, 14, 124 006, 430 2019.

Grise, K. M. and Davis, S. M.: Hadley cell expansion in CMIP6 models, Atmospheric Chemistry and Physics, 20, 5249–5268, 2020.

Harrison, S., Bartlein, P., Brewer, S., Prentice, I., Boyd, M., Hessler, I., Holmgren, K., Izumi, K., and Willis, K.: Climate model benchmarking with glacial and mid-Holocene climates, Climate Dynamics, 43, 671–688, 2014.

Haug, G. H., Hughen, K. A., Sigman, D. M., Peterson, L. C., and Rohl, U.: Southward migration of the intertropical convergence zone 435 through the Holocene, Science, 293, 1304–1308, 2001.

Herbert, A. V. and Harrison, S. P.: Evaluation of a modern-analogue methodology for reconstructing Australian palaeoclimate from pollen, Review of Palaeobotany and Palynology, 226, 65–77, 2016.

Hill, S. A.: Theories for past and future monsoon rainfall changes, Current Climate Change Reports, 5, 160–171, 2019.

Hill, S. A., Ming, Y., Held, I. M., and Zhao, M.: A moist static energy budget–based analysis of the Sahel rainfall response to uniform oceanic 440 warming, Journal of Climate, 30, 5637–5660, 2017.

Holmes, J. A.: How the Sahara became dry, Science, 320, 752–753, 2008.

Hopcroft, P. O. and Valdes, P. J.: On the role of dust-climate feedbacks during the mid-Holocene, Geophysical Research Letters, 46, 1612–1621, 2019.

Huntley, B.: Reconstructing palaeoclimates from biological proxies: some often overlooked sources of uncertainty, Quaternary Science 445 Reviews, 31, 1–16, 2012.

Jungandreas, L., Hohenegger, C., and Claussen, M.: How does the explicit treatment of convection alter the precipitation–soil hydrology interaction in the mid-Holocene African humid period?, Climate of the Past, 19, 637–664, 2023.

Kang, S. M. and Lu, J.: Expansion of the Hadley cell under global warming: Winter versus summer, Journal of Climate, 25, 8387–8393, 2012.

450 Kang, S. M., Shin, Y., and Xie, S.-P.: Extratropical forcing and tropical rainfall distribution: energetics framework and ocean Ekman advection, npj Climate and Atmospheric Science, 1, 20 172, 2018.

Kaufman, D. S. and Broadman, E.: Revisiting the Holocene global temperature conundrum, Nature, 614, 425–435, 2023.

Lau, W. K. and Kim, K.-M.: Robust Hadley circulation changes and increasing global dryness due to CO2 warming from CMIP5 model projections, Proceedings of the National Academy of Sciences, 112, 3630–3635, 2015.

455 Lim, S., Chase, B. M., Chevalier, M., and Reimer, P. J.: 50,000 years of vegetation and climate change in the southern Namib Desert, Pella, South Africa, Palaeogeography, Palaeoclimatology, Palaeoecology, 451, 197–209, 2016.

Lionello, P., D'Agostino, R., Ferreira, D., Nguyen, H., and Singh, M. S.: The Hadley circulation in a changing climate, Annals of the New York Academy of Sciences, 1534, 69–93, 2024.

Liu, S., Jiang, D., and Lang, X.: Mid-Holocene drylands: A multi-model analysis using Paleoclimate Modelling Intercomparison Project
460   phase III (PMIP3) simulations, The Holocene, 29, 1425–1438, 2019.

Lowry, A. L. and McGowan, H. A.: Insights into the Australian mid-Holocene climate using downscaled climate models, Climate of the
     Past, 20, 2309–2325, 2024.

Lu, J., Vecchi, G. A., and Reichler, T.: Expansion of the Hadley cell under global warming, Geophysical Research Letters, 34, 2007.

McGee, D., Donohoe, A., Marshall, J., and Ferreira, D.: Changes in ITCZ location and cross-equatorial heat transport at the Last Glacial
465   Maximum, Heinrich Stadial 1, and the mid-Holocene, Earth and Planetary Science Letters, 390, 69–79, 2014.

Milly, P. C. and Dunne, K. A.: Potential evapotranspiration and continental drying, Nature Climate Change, 6, 946–949, 2016.

Nagai, R. H., Sousa, S. H. d. M., Burone, L., and Mahiques, M. M. d.: Paleoproductivity changes during the Holocene in the inner shelf of
     Cabo Frio, southeastern Brazilian continental margin: Benthic foraminifera and sedimentological proxies, Quaternary International, 206,
     62–71, 2009.

470 Nguyen, H., Evans, A., Lucas, C., Smith, I., and Timbal, B.: The Hadley circulation in reanalyses: Climatology, variability, and change,
     Journal of Climate, 26, 3357–3376, 2013.

Nicholson, S. E.: Dryland climatology, 2011.

Otto-Bliesner, B. L., Braconnot, P., Harrison, S. P., Lunt, D. J., Abe-Ouchi, A., Albani, S., Bartlein, P. J., Capron, E., Carlson, A. E., Dutton,
     A., et al.: The PMIP4 contribution to CMIP6–Part 2: Two interglacials, scientific objective and experimental design for Holocene and Last
475   Interglacial simulations, Geoscientific Model Development, 10, 3979–4003, 2017.

Pausata, F. S., Messori, G., and Zhang, Q.: Impacts of dust reduction on the northward expansion of the African monsoon during the Green
     Sahara period, Earth and Planetary Science Letters, 434, 298–307, 2016.

Pausata, F. S., Gaetani, M., Messori, G., Berg, A., de Souza, D. M., Sage, R. F., and DeMenocal, P. B.: The greening of the Sahara: Past
     changes and future implications, One Earth, 2, 235–250, 2020.

480 Pikovnik, M., Zaplotnik, Ž., Boljka, L., and Žagar, N.: Metrics of the Hadley circulation strength and associated circulation trends, Weather
     and Climate Dynamics, 3, 625–644, 2022.

Prado, L. F., Wainer, I., Chiessi, C. M., Ledru, M.-P., and Turcq, B.: A mid-Holocene climate reconstruction for eastern South America,
     Climate of the Past, 9, 2117–2133, 2013.

Proske, U., Heslop, D., and Haberle, S.: A Holocene record of coastal landscape dynamics in the eastern Kimberley region, Australia, Journal
485   of Quaternary Science, 29, 163–174, 2014.

Reeves, J. M., Bostock, H. C., Ayliffe, L. K., Barrows, T. T., De Deckker, P., Devriendt, L. S., Dunbar, G. B., Drysdale, R. N., Fitzsim-
     mons, K. E., Gagan, M. K., et al.: Palaeoenvironmental change in tropical Australasia over the last 30,000 years–a synthesis by the
     OZ-INTIMATE group, Quaternary Science Reviews, 74, 97–114, 2013.

Scheff, J., Mankin, J. S., Coats, S., and Liu, H.: CO2-plant effects do not account for the gap between dryness indices and projected dryness
490   impacts in CMIP6 or CMIP5, Environmental Research Letters, 16, 034 018, 2021.

Scheff, J., Coats, S., and Laguë, M. M.: Why do the global warming responses of land-surface models and climatic dryness metrics disagree?,
     Earth's Future, 10, e2022EF002 814, 2022.

Schneider, T., Bischoff, T., and Haug, G. H.: Migrations and dynamics of the intertropical convergence zone, Nature, 513, 45–53, 2014.

Seager, R. and Henderson, N.: Diagnostic computation of moisture budgets in the ERA-Interim reanalysis with reference to analysis of
495   CMIP-archived atmospheric model data, Journal of Climate, 26, 7876–7901, 2013.

Taylor, K. E.: Summarizing multiple aspects of model performance in a single diagram, Journal of geophysical research: atmospheres, 106, 7183–7192, 2001.

Thompson, A. J., Zhu, J., Poulsen, C. J., Tierney, J. E., and Skinner, C. B.: Northern Hemisphere vegetation change drives a Holocene thermal maximum, Science advances, 8, eabj6535, 2022.

500 Tierney, J. E., Pausata, F. S., and deMenocal, P. B.: Rainfall regimes of the Green Sahara, Science Advances, 3, e1601 503, 2017.

Watt-Meyer, O. and Frierson, D. M.: ITCZ width controls on Hadley cell extent and eddy-driven jet position and their response to warming, Journal of Climate, 32, 1151–1166, 2019.

Wirtz, K. W., Lohmann, G., Bernhardt, K., and Lemmen, C.: Mid-Holocene regional reorganization of climate variability: Analyses of proxy data in the frequency domain, Palaeogeography, Palaeoclimatology, Palaeoecology, 298, 189–200, 2010.

505 Wu, M., Li, C., and Zhang, Z.: Recalibrated projections of the Hadley circulation under global warming, Environmental Research Letters, 19, 104 041, 2024.

Yang, Y. and Roderick, M. L.: Radiation, surface temperature and evaporation over wet surfaces, Quarterly Journal of the Royal Meteorological Society, 145, 1118–1129, 2019.

Yang, Y., Roderick, M. L., Zhang, S., McVicar, T. R., and Donohue, R. J.: Hydrologic implications of vegetation response to elevated CO_2
510 in climate projections, Nature Climate Change, 9, 44–48, 2019.